Comprehensive Numerical Modeling of Filamentary RRAM Device

D. Niraula*, V. Karpov
Department of Physics and Astronomy, The University of Toledo, Toledo, OH, USA
*Corresponding author: 2801 W. Bancroft St., MS 111, Toledo, OH, 43606, USA
dipesh.niraula@rockets.utoledo.edu

Abstract: We present a numerical modeling of resistive random-access memory (RRAM) consisting of ON and OFF device states which mutually transforms through SET (ON→OFF) and RESET (OFF→ON) switching. ON and OFF states corresponds to presence and absence of conducting filament and SET and RESET processes corresponds to formation and destruction of the conducting filament. Thermodynamics dictate that the states correspond to the minimum of free energy and thus the processes correspond to minimization. Accordingly, we devised a program in MATLAB® package that simulates RRAM. The program consists of four modules constructed in COMSOL Multiphysics® modeling software package representing the device states and switching processes which are sequentially executed according to actual switching sequence. Each module solves the electrodynamic and heat transfer equations yielding RRAM free energy and I-V. Additionally, our modeling accounts for the non-crystallinity of the filamentary structure yielding I-V with ramp-rate dependence and cycle-to-cycle variation.

Keywords: Device Modeling, RRAM, Resistive Switching, Thermodynamics of Phase Transition, Double Well Potential, Variability

1. Introduction

RRAM is a capacitor-like nanoscale device, sketched in Figure 1 (top left). It operates via resistive switching between the insulating and conducting states in response to external bias. The switching is due to formation or destruction of a conducting filament in its insulating layer. The corresponding conducting (ON) and insulating (OFF) states represent the logical '1' and '0' binary states.

Figure 1 (right) depicts a typical RRAM current-voltage (I-V) characteristics which consists of several domains related to device states and switching processes. The domains C-0-D and A-0-F correspond to the ON and OFF states remaining intact under source voltage ramping, whereas, A-B-C and D-E-F reflect structural changes in response to voltage ramping representing respectively the SET and RESET switching processes. The characteristic features of the switching processes are the voltage snapback A-B followed by the vertical domain B-C for SET, and the voltage snapforward D-E followed by the horizontal domain E-F for RESET.

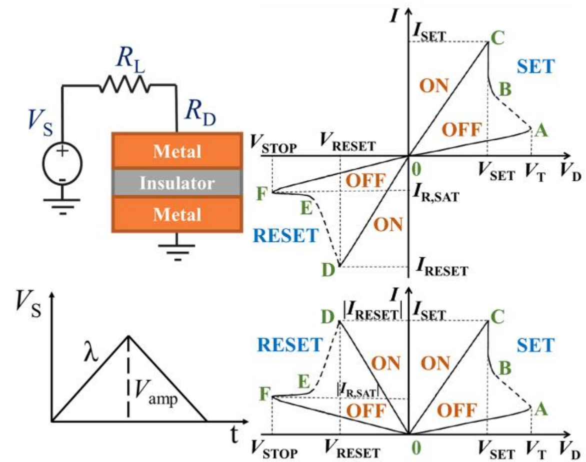

Figure 1. Top left: Schematic of the circuitry where source voltage V_S, load resistor R_L, and a generic RRAM device R_D is connected in series. Bottom left: Plot of the pulsed source voltage where λ and V_{amp} are the ramp-rate and amplitude. Top right: Representation of a typical I-V characteristics of RRAM [1-4]. Bottom right: Customary representation of the I-V with absolute-valued current axis. V_D is the voltage drop across the RRAM device and V_T is the threshold voltage. SET current I_{SET} is the maximum current limited by V_{amp} and stop voltage V_{STOP} is the maximum device voltage, during RESET, limited by V_{amp} of opposite polarity. The dashed domains represent nucleation event.

In this paper, we present a comprehensive numerical model of RRAM [5] devised in COMSOL and MATLAB (communicates with each other via LiveLink™ for MATLAB®), based on our thermodynamic description [6, 7]. As a unique feature, our numerical model incorporates the configurational disorder present in non-crystalline materials simulating the observed voltage ramp-rate dependency and cycle-to-cycle variation.

2. Physics of Device Operation

When the bias exceeds a certain threshold voltage, a needle-shaped embryo nucleates in the insulator layer. It grows longitudinally into a conducting filament which shunts the device and then further grows radially, during which process the device resistance becomes reciprocal of current corresponding to the I-V domain B-C. The filament has a finite capacitance and thus accumulates charges. The charged filament creates radial polarization that freezes upon the completion of SET process and remains intact in the ON state. The polarization-charge interaction decreases the filament energy. RESET is carried out by reversing the bias polarity during which the filament charges oppositely making the earlier created frozen polarization energetically unfavorable. When the magnitude of the reversed bias gets sufficiently large, the polarization-charge interaction increases the system energy enough to break the filament introducing the insulating gap and sending the device back to the insulating OFF state. Figure 2 depicts the switching mechanism.

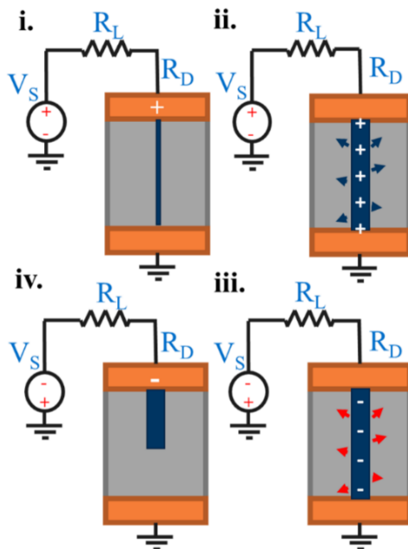

Figure 2. Formation and dissolution of the conducting filament in a generic RRAM device. The arrows represent polarization of the insulating host near charged filament; blue (ii) and red (iii) color denotes energetically favorable and unfavorable states, respectively. Note: the pictures are placed in cyclic order corresponding the switching cycle.

We applied the thermodynamics of phase transition to quantify the switching process. Thermodynamics is applicable in nano-sized RRAM because of the very short thermalization time, faster than the switching time, so the system is approximately in thermal equilibrium. Thermodynamics describe that when the device is subjected to external electric stress, phase transformation takes place to minimize the system energy. A minimum of three phases are necessary to describe the bipolar switching: insulating (i), unstable conducting (uc), and metastable conducting (mc), as shown in Figure 3. The long-lived conducting filament is composed of mc-phase which transforms to the stable i-phase during RESET via the uc-phase and vice-versa during SET. The difference in chemical potential between the three phases are the model adjustable parameters.

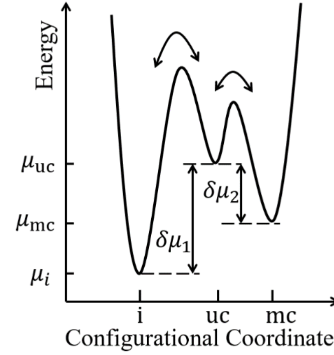

Figure 3. One dimensional representation of the system chemical potentials in unspecified configurational coordinates showing three distinct minima corresponding to the i, uc, and mc phases and their related barrier. Arrows represent transformations between the mc and uc, and the uc and i phases where the energy barriers are relatively low.

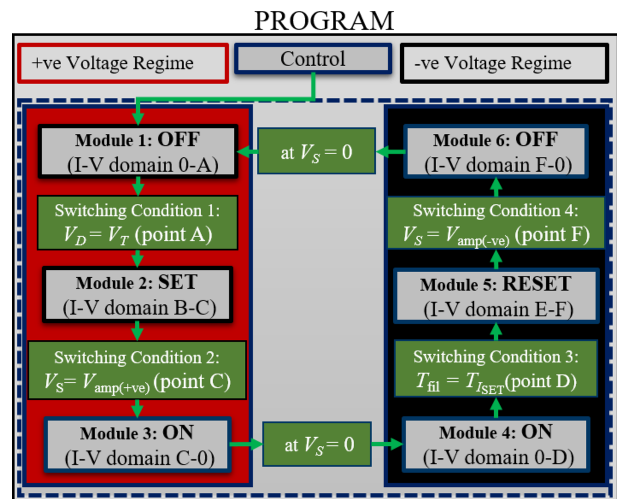

Figure 4. Flowchart of the program that simulates RRAM I-V characteristics.

3. Numerical Model

The device I-V in Figure 1 (right) consists of the ON and OFF device states and the SET and RESET switching processes. To simulate the device operation, we devised a program in MATLAB as shown in Figure 4, that consists of the control, modules, and switching conditions. The control is the 'brain' of the program executing the modules in sequence when the corresponding switching conditions are satisfied. The

modules refer to the different device states and switching processes and can be naturally divided into positive and negative polarity regimes representative of the actual bipolar switching sequence. A brief description of the program, its modules and switching conditions are presented in Table 1.

Table 1: Brief description of the Modules (**M**) & Switching Conditions (**SC**)

M1: OFF (I-V Domain 0-A) Simulation begins, partial filament containing a gap, source voltage (V_S) pulse is ascending in time
SC1: $V_D = V_T$ (Point A) Program switches to SET module (physically, filament nucleates in the gap) when the device voltage (V_D) exceeds to the threshold voltage [8] given by, $V_T \cong \tilde{V}\left[\ln\left(\frac{\tilde{V}}{\lambda\tau_0}\right)\right]$, where $\tilde{V} = \frac{hW_0}{kT}\sqrt{\frac{3\pi^2\alpha^3\Lambda W_0}{32\epsilon r_c^3}}$ and h: filament height, W_0: nucleation barrier, α: ratio of minimum filament radius to critical nucleus radius (r_c), Λ: embryo aspect ratio dependent logarithmic multiplier, λ: source voltage ramp-rate, τ_0: atomic-vibration time, and ε: dielectric permittivity
M2: SET (I-V Domain B-C) Filament evolves radially with ascending positive voltage source governed by thermodynamics
SC2: $V_S = V_{amp(+ve)}$ (Point C) SET process ceases when the source voltage pulse reaches its peak amplitude ($V_{amp(+ve)}$) where +ve represent the positive voltage polarity
M3 & M4: ON (I-V Domain C-0-D) ON module begins with the descending part of the input pulse, during which the filament "freezes" and stabilizes. The filament radius equals to that at $V_{amp(+ve)}$. The fourth module, also an ON module, starts with ascending negative input pulse.
SC3: $T_{fil} = T_{ISET}$ (Point D) Since the filament remains intact during ON state, so does its resistance. Thus, the filament unfreezes when the filament temperature equals to the filament temperature (T_{fil}) at I_{SET} (device current at $V_{amp(+ve)}$), i.e. T_{ISET}, and breaks driven by the unfavorable polarization of the insulating host beginning the RESET process.
M5: RESET (I-V Domain E-F) the gap evolves longitudinally with ascending negative voltage source governed by thermodynamics
SC4: $V_S = V_{amp(-ve)}$ (Point F) RESET process ceases when the source voltage reaches its peak amplitude ($V_{amp(-ve)}$)
M6: OFF (I-V Domain F-0) OFF module begins with descending input pulse, during which the gap stabilizes. The gap width equals to the that at $V_{amp(-ve)}$.

**This completes one complete switching cycle. **

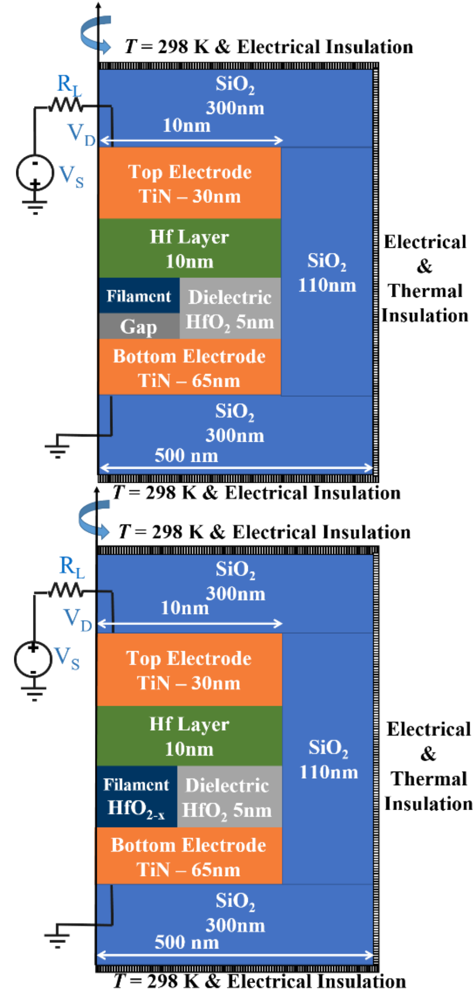

Figure 5. Schematic of multi-layered RRAM cross-section. Top and bottom figures correspond to device model used to emulate OFF/RESET and ON/SET respectively. The figures include geometric parameters and material names of the devices' various layers, and the boundary conditions. Note: figures not drawn to scale.

3.1 Device Model

We selected TiN/Hf/HfO_2/TiN multi-layered RRAM device having a cross-section area of 20nm×20nm as reported in [1, 9]**;** however, a modified cylindrical geometry of 10 nm radius was considered and built in *2D Axisymmteric Space Dimension* instead, as shown in Figure 5, to reduce the 3D geometry to 2D by exploiting the axial rotational symmetry the cylindrical shape. Figure 5 (top) corresponds to OFF state and RESET process, whereas, Figure 5 (bottom) to ON state and SET process. Although the OFF state and RESET process utilize the same device structure, the gap remains fixed throughout OFF state but evolves longitudinally during RESET process. Similarly, the filament remains fixed throughout ON

state but evolves radially during RESET process. More step-by-step instruction can be found in [5].

The evolution of filament and gap during SET and RESET is quantified by finding the minimum free energy configuration with respect to the filament radius and gap height. The free energy consists of thermal, electrostatic, and phase (surface and volume) energy,

$$F_{SET} = \iint \rho C_P \delta T drdz + \frac{1}{2}\iint \epsilon |E|^2 drdz + 2\pi r h \sigma_s + \pi r^2 h \delta\mu_1 \qquad (1.1)$$

$$F_{RESET} = \iint \rho C_P \delta T drdz + \frac{1}{2}\iint \epsilon |E|^2 drdz + 2\pi r l \sigma_s + \pi r^2 l \delta\mu_2 \qquad (1.2)$$

where, ρ is the mass density, C_p is the specific heat capacity at constant pressure, δT is the change in temperature, ε is the permittivity, $\boldsymbol{E}$ is the electric field, r and h is the filament radius and height, l is the gap width, σ_s is the interfacial energy, and $\delta\mu_1$ is the difference in chemical potential between the uc-phase and i-phase and $\delta\mu_2$ between the uc-phase and mc-phase. The details of the minimization process have been presented in our 2017 COMSOL conference proceeding [10] and in [5] with additional modification.

To obtain the temperature and electric field distribution necessary to calculate the free energy for switching process and the I-V characteristics for both the switching process and device states, we solved the differential equations listed in Table 2. Note that since thermodynamics apply for equilibrium state, static equations are solved for SET and RESET process for dc power sources in discrete increments whereas time-dependent equations are solved for ON and OFF states with pulsed source.

Table 2: Utilized COMSOL Modules and Differential Equations

OFF/ON	SET/RESET
Electric Currents module	
$\nabla . \boldsymbol{J} = 0$, $\boldsymbol{J} = \sigma_c \boldsymbol{E} + \epsilon \frac{\partial \boldsymbol{E}}{\partial t}$, $\boldsymbol{E} = -\nabla V$	$\nabla . \boldsymbol{J} = 0$, $\boldsymbol{J} = \sigma_c \boldsymbol{E}$, $\boldsymbol{E} = -\nabla V$
Heat Transfer in Solids module	
$\rho C_p \frac{\partial T}{\partial t} - \nabla . (\kappa \nabla T) = Q_s$	$-\nabla . (\kappa \nabla T) = Q_s$
Multiphysics module	
$Q_s = \boldsymbol{J} . \boldsymbol{E}$	$Q_s = \boldsymbol{J} . \boldsymbol{E}$

**Additionally, *Electric Circuit* module is used to define the circuitry. **

Here $\boldsymbol{J}$ is the current density, σ_c is the electric conductivity, $\boldsymbol{E}$ is the electric field, κ is the thermal conductivity, and Q_s is the heat source. The equations under *Electric Currents* modules are respectively current conservation law, Ohm's law, and the relation between electric field and potential due to Maxwell Law, followed by the Fourier heat law under *Heat transfer in Solid* module where the heat source is given by Joule heating coupled by the *Multiphysics* module.

The boundary conditions are listed below:

i. *Electric Insulation* ($\boldsymbol{n}.\boldsymbol{J} = 0$)
All three boundaries of the SiO_2 domain are electrically insulated. Here $\boldsymbol{n}$ is the unit vector normal to the surface boundary.

ii. *Ground (V = 0)*
Interface common to the bottom electrode and SiO_2 substrate is grounded.

iii. *Terminal* ($V = V_D$ or $I = I_S$)
Interface common to the top electrode and SiO_2 superstrate is connected to the power-source and load resistor in series. *Terminal* handles both voltage and current source.

iv. *Temperature* ($T = 298\ K$)
Free surfaces of the superstrate and substrate SiO_2 layers are placed at room temperature, assuming they are in contact with a larger body which acts as a heat sink and maintains room temperature. Also, all three boundaries of the SiO_2 domain are at room temperature.

v. *Diffuse Surface* ($-\boldsymbol{n}.\boldsymbol{q} = \sigma_B (T_{amb}^4 - T^4)$)
All the interface and boundary of the device loses heat through radiation governed by Stefan-Boltzmann law. Here q is the power radiated per surface area, σ_B is the Stefan-Boltzmann constant, and T_{amb} is the ambient temperature (298 K).

3.2 Conduction Mechanism

Electric Conduction: There is lack of consensus on the conduction mechanism of filamentary RRAM [11] in the RRAM community. Various models, such as Poole-Frenkel [12-14], trap-assisted tunneling, [12, 15-17] Schottky emission, [18-20] space charge limited current, [21] and hopping [22, 23] have been proposed to for similar HfO_2 RRAM structures. Here, we tried several of the above mechanisms, all working well enough and offering no preferences in I-V modeling. At the end, for the sake of its novelty to the community, for this work, we chose phonon assisted hopping through the optimum hopping chains [24,25]

$$\sigma_{c(f,g)} = \sigma_{0(f,g)} \exp\left(-\frac{E_{G(f,g)}}{kT}\right) \exp\left(\sqrt{\frac{eV}{kT}}\right) \qquad (2)$$

where, subscript *f* and *g* pertains to filament and gap, E_G is the energy difference between the Fermi-level and mobility edge. The temperature and voltage dependence were introduced in COMSOL via *variables* under *Component Definitions*.

Thermal Conduction: Widemann-Franz-Lorenz law was applied to define thermal conductivity of the metal electrodes and filament similar to [26]. The law was applied as well to the gap thermal transport where the electric conductivity is higher than that of typical insulator similar to [27].

Ballistic Heat Transport: One anomaly discovered in this modeling was 'unphysically' high (~4500K) temperature of the gap, well above the melting temperature of HfO_2 (2274°C [28]) and other transitional metal oxides [28]. Similar temperature was reported for the TaO_x device model in [29] where the Poole-Frenkel conduction mechanism was employed, however it remained unrecognized as a red flag.

We have verified that such an 'unphysical' temperature is due to the assumed diffusive heat transport. The problem is solved by noticing that the electrons can travel through the very thin gap dielectrics ballistically, and each electron carries its corresponding portion of Joule heat away from the gap. It has been observed indeed [30] that the energy relaxation length of the electron in amorphous SiO_2 is on the order of 10 nm; similar lengths must correspond to HfO_2 and other non-crystalline materials. Since, the energy relaxation length is greater than the gap width, most of the energy is dissipated away from the gap. To account for the ballistic transport, we introduced the dimensionless corrective coefficient, κ_{eff} defined as the ratio of energy relaxation length in the ballistic heat transfer (~ 10 nm) to that of diffusive heat transfer (~ 1 nm). That procedure allowed us to 'cool down' the gap below 1500 K.

4. Variability of RRAM Parameters: Role of Disorder

The material non-crystallinity is one of the most common features of transition metal oxide based RRAM. In a non-crystalline material, some atoms or group of atoms retain their mobility by being able to move between more than one equilibrium positions, sufficiently described in terms of double well potentials (DWP) [31-34]**,** The significance of DWP is that, depending on their configuration, they will exert various forces on the system changing the material

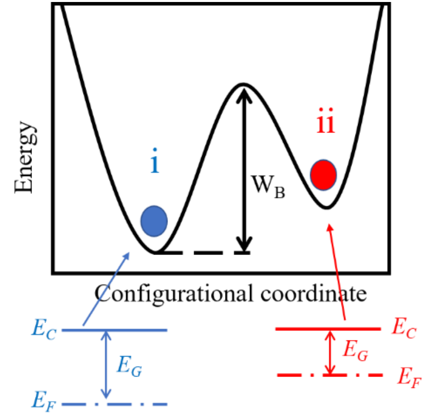

Figure 6. Schematic of a double well potential representing two configurations, separated by a barrier height of energy WB. Each configuration is associated with different deformation potentials and thus different band gaps.

properties such as electrical conductivity, chemical potentials and others.

Figure 6 represents an energy diagram of a DWP, having an energy barrier of random height W_B. The corresponding relaxation time is given by,

$$\tau = \tau_0 \exp\left(\frac{W_B}{kT}\right), \qquad \text{i.e. } W_B(\tau) = kT \ln\left(\frac{\tau}{\tau_0}\right). \quad (3)$$

Given a certain relaxation time τ, only DWP with barriers below $W_B(\tau)$ can make an inter-well transition and contribute to a process

In the following subsection, we show how the application of DWP in the modeling correctly simulates the ramp-rate dependency and cycle-to-cycle variation observed in RRAM I-V characteristics.

Average Ramp-Rate Dependent Effects: Let τ be the voltage pulse time, which is the reciprocal of the ramp-rate λ. The active DWP fractional concentration,

$$f(\tau) = \frac{kT}{\Delta W_B} \ln\left(\frac{\tau}{\tau_{\min}}\right), \qquad \text{for } \tau_{\min} < \tau < \tau_{\max}, (4)$$

is obtained by integrating the relaxation-time distribution from $\tau_{\min}$ to τ [9, 31]**.** Furthermore, the relaxation-time is obtained from the uniformly distributed random barrier heights distribution in a certain interval $\Delta W_B = W_{B,\max} - W_{B,\min}$, where the maximum and minimum barrier heights corresponds to $\tau_{\max}$ and $\tau_{\min}$. The active DWPs affect the system conductivity as illustrated in Figure 6.

The relative volume change (dilation) is proportional to the activated DWP fraction,

$$u(\tau) = u_0 f(\tau). \quad (5)$$

The deformation dependent activation energy of conduction is given by,

$$E_F \approx \langle E_F \rangle + Du, \qquad \text{where,} \qquad D \equiv \frac{dE_F}{du}, \quad (6)$$

where D is the deformation potential. Thus, the resistance becomes,

$$R \propto \exp\left[\alpha \ln\left(\frac{\tau}{\tau_{\min}}\right)\right], \text{where}, \alpha \equiv \frac{u_0 D}{\Delta W_B}. \quad (7)$$

In addition, the changes in free energy depend on the differences in chemical potentials presented Figure 3. We consider that the transitions in DWP will change these free energy differentials, which results in,

$$\delta\mu_{1,2} = \overline{\delta\mu_{1,2}} + \beta_{1,2} kT\left(\frac{1}{\Delta W_{Buc}} - \frac{1}{\Delta W_{Bi,mc}}\right)\ln\frac{\tau}{\tau_{\min}}. \, (8)$$

Here $\overline{\delta\mu_1}$ and $\overline{\delta\mu_2}$ represent DWP independent contributions, and β_1 and β_2 are proportionality coefficients, to be adjusted in the course of modeling.

Cycle-to-Cycle Variations: The distributions in Eq. (4) imply large enough systems where the statistics of DWP does not depend in the system size. However, in nano-size small structure of modern RRAM, the number of DWP is not large enough to sufficiently present their full spectrum. Such scarcity makes it possible that different nominally identical structures will have quite different DWP ensembles showing significant variability between their parameters.
Cycle-to-cycle variations find their natural explanations along the same lines because each switching cycle creates the amorphous portion of the device anew. As a result, every switching cycle under nominally identical conditions yields different microscopic structures. That differences cause variations in DWP barrier heights, chemical potentials, and deformation potentials causing cycle-to-cycle variations in the I-V characteristics.

To account for the latter type of variations, we have applied random number generator to randomly vary the DWP ensembles in a device from once cycle to another. We however ensured that the random selection is made from the 'parental' database where all DWP are represented with relative weights as presented in Table 4 under Static Disorder.

Our numerical model closely reproduces the observed I-V characteristics including both the ramp-rate and cycle-to-cycle variations as shown in Figure 7. The top figure shows I-V for three different voltage ramp-rate: 100 V/s, 10 kV/s, and 1 MV/s. Notice that the threshold and SET voltage increases with ramping rate, so as the RESET saturation current and Stop voltage, consistent with the observation. The bottom figure shows I-V characteristics for 10 switching

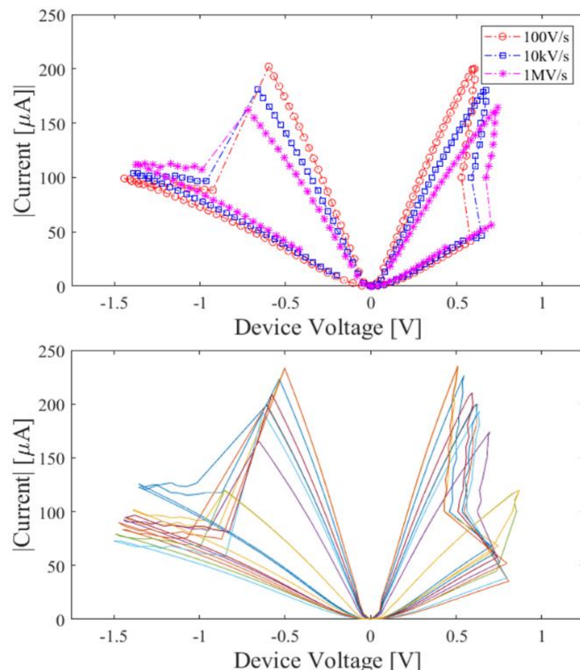

Figure 7. Plot of the simulated I-V characteristics. Top plot shows the I-V for various ramp-rate and the bottom plot shows I-V for 10 different switching cycles.

cycles at 100V/s ramp-rate, reproducing the cycle-to-cycle variations.

5. Conclusion

We list several achievements,

1. Developed a physics based numerical model of RRAM device in COMSOL and MATLAB that closely reproduces I-V characteristics of a real device
2. The non-trivial features of our model lie in the overlap of the device smallness and its non-crystallinity.
3. The ballistic nature of the electron transport through an amorphous dielectric gap is essential.
4. The effects of double well atomic potential characteristic of amorphous structures lead to strong variations of parameters between nominally identical RRAM structures.
5. The thermodynamic description (as a great simplification of the generally required kinetic approach) is shown to be sufficient for modeling the nano-size small modern devices.

References

[1] A. Fantini, et al., Intrinsic Switching Behavior in HfO_2 RRAM by Fast Electrical Measurements on Novel 2R Test Structures, *2012 4th IEEE International Memory Workshop, Milan*, pp. 1-4 (2012).

[2] D. J. Wouters, et al., Analysis of Complementary RRAM Switching, *IEEE El. Dev. Letts.*, **33**, pp. 1186-1188 (2012).

[3] Y. Y. Chen, et al., Understanding of the endurance failure in scaled HfO2-based 1T1R RRAM through vacancy mobility degradation, *2012 International Electron Devices Meeting, San Francisco, CA*, pp. 20.3.1-20.3.4 (2012).

[4] S. Ambrogio, et al., Statistical Fluctuations in HfO_x Resistive-Switching Memory: Part I - Set/Reset Variability, *IEEE Trans. El. Dev.*, **61**, pp. 2912-2919 (2014).

[5] D. Niraula, et al., Comprehensive numerical modeling of filamentary RRAM devices including voltage ramp-rate and cycle-to-cycle variations, *J. Appl. Phys*. (2018) (Submitted) arXiv:1806.01397 [cond-mat.mes-hall].

[6] V. Karpov, et al., Thermodynamic analysis of conductive filament, *Appl. Phys. Letts.*, **109**, 093501 (2016).

[7] V. G. Karpov, et al., Thermodynamics of phase transitions and bipolar filamentary switching in resistive random-access memory, *Phys. Rev. Appl.*, **8**, 024028 (2017).

[8] V. G. Karpov, et al., Field induced nucleation in phase change memory, *Phys. Rev. B*, **78**, 052201 (2008).

[9] A. Fantini, et al., Intrinsic switching variability in HfO2 RRAM, *2013 5th IEEE International Memory Workshop, Monterey, CA*, pp. 30-33 (2013).

[10] D. Niraula et al., Numerical modeling of resistive switching in RRAM device, *Proceedings of the 2017 COMSOL Conference in Boston* (2017).

[11] E. W. Lim et al., Conduction Mechanism of Valence Change Resistive Switching Memory: A Survey, *Electronics*, **4**, 586-613 (2015).

[12] B. Long, et al., Switching dynamics and charge transport studies of resistive random-access memory devices, *Appl. Phys. Lett*., **101**, 113503 (2012).

[13] R. Mahapatra, et al., Temperature impact on switching characteristics of resistive memory devices with HfOx/TiOx/HfOx stack dielectric, *Microelectronic Engineering*, **138**, 118121, (2015).

[14] C. Walczyk, et al., Impact of Temperature on the Resistive Switching Behavior of Embedded HfO2-Based RRAM Devices, *IEEE Trans. On El. Dev*., **58**, 3124 (2011).

[15] F. M. Puglisi, et al., A Complete Statistical Investigation of RTN in HfO2-Based RRAM in High Resistive State, *IEEE Trans. On El. Dev.,* **62**, 2606 (2015).

[16] S. Yu, et al., Conduction mechanism of TiN/HfOx/Pt resistive switching memory: A trap-assisted tunneling model, *Appl. Phys. Lett*., **99**, 063507 (2011).

[17] G. Bersuker, et al., Grain boundary-driven leakage path formation in HfO_2 dielectrics, *Solid-State Electronics*, **65-66**, 146150 (2011).

[18] J.-K. Lee, et al., Accurate analysis of conduction and resistive switching mechanisms in doublelayered resistive-switching memory devices, *Appl. Phys. Lett.*, **101**, 103506 (2012). ON-Schottky Emission,

[19] Y.-E. Syu, et al., Atomic-level quantized reaction of HfOx memristor, *Appl. Phys. Lett.,* **102**, 172903 (2013).

[20] O. Khaldi, et al., Investigation of electrical properties of HfO_2 metal-insulator-metal (MIM) devices, *Appl. Phys. A*, **116**, 16471653 (2014).

[21] H. Y. Lee, et al., Low-Power and Nanosecond Switching in Robust Hafnium Oxide Resistive Memory with a Thin Ti Cap, *IEEE El. Dev. Lett*., **31**, 44 (2010).

[22] R. Fang, et al., Low-Temperature Characteristics of HfOx-Based Resistive Random Access Memory *IEEE El. Dev. Lett.,* **36**, 567 (2015).

[23] D. C. Sekar, et al., Technology and circuit optimization of resistive RAM for low-power, reproducible operation, *2014 IEEE International Electron Devices Meeting, San Francisco*, *CA,* 2014.

[24] B. I. Shklovskii, Nonohmic hopping conduction, *Sov. Phys. Semicond*., **10(8)**, 855 (1976).

[25] E. I. Levin, et al., Transverse hopping conductivity of amorphous films in strong electric fields, *Sov. Phys. Semicond.*, **22(4)**, 407 (1988).

[26] D. Niraula et al., Heat Transfer in Filamentary RRAM Devices, *IEEE Trans. On El. Dev*., **64**, 4106 (2017).

[27] D. L. Kencke, et al., The role of interfaces in damascene phase-change memory, *IEDM Tech. Dig.*, *Dec. 2007*, pp. 323-326 (2007).

[28] Carl L. Yaws. *The Yaws Handbook of Physical Properties for Hydrocarbons and Chemicals,* 2nd ed. Gulf Professional Publishing, Houston, TX (2015).

[29] D. Li, et al., Scaling behavior of oxide-based electrothermal threshold switching devices, *Nanoscale*, **9**, 14139 (2017).

[30] T. Toita, et al., Energy Relaxation Length for Ballistic Electron Transport in SiO_2, *Phys. Stat. Sol.(b)*, **204**, 129 (1997).

[31] I. V. Karpov, et al., Fundamental drift of parameters in chalcogenide phase change memory, J. Appl. Phys., 102, 124503 (2007).

[32] J. Frenkel, *Kinetic Theory of Liquids*, Clarendon Press, Oxford. 1946.

[33] P. W. Anderson, et al., Anomalous low temperature thermal properties of glasses and spin glasses, *Philosophical Magazine*, **25**, 1 (1972).

[34] Yu. M. Galperin, et al., Localised states in glasses, *Advances in Physics*, **38**, 669 (1989).

Acknowledgement

This work was supported in part by the Semiconductor Research Corporation (SRC) under Contract No. 2016-LM-2654.

Appendix

List of all the parameter values used in the modeling.

Table 3: Material Parameters

Material	σ_c[S/m]	κ[W/K.m]	C_P[J/kg.K]	ϵ_r[c]	ρ[kg/m^3]
SiO_2	10^{-9}	1.38	703	3.9	2.2×10^3
TiN	Exp. $\sigma_c(T)$[a]	$\sigma_c(T)TL$[d]	545.33	$-\infty$[f]	5.22×10^3
Hf	Exp. $\sigma_c(T)$[b]	$\sigma_c(T)TL$[d]	144	$-\infty$[f]	13.3×10^3
HfO_2	10	0.5	120	25	10×10^3
HFO_{2-x}	$\sigma_{0f}\exp\left(-\alpha_f \ln\left(\frac{\tau}{\tau_0}\right)\right)\exp\left(\sqrt{\frac{eV}{kT}}\right)$	$\sigma_c(T)TL$[d]	140[e]	$-\infty$[e,f]	12×10^3[e]
Gap	$\sigma_{0g}\exp\left(-\alpha_g \ln\left(\frac{\tau}{\tau_0}\right)\right)\exp\left(\sqrt{\frac{eV}{kT}}\right)$	$\kappa_{\text{eff}}\sigma_c(T)TL$[d]	120	25	10×10^3

[a] E. Langereis et al., *J. Appl. Phys.* **100,** 023534 (2006).
[b] P. D. Desal, et al., *J. Phys. Chem. Ref. Data.* **3**, 1069 (1984).
[a, b] the experimental data points were inserted in COMSOL via *interpolation function*

[c] Relative Permittivity
[d] Wiedemann-Franz-Lorenz Law
[e] Assumed value such that it lies in between Hf and HfO_2
[f] -10^6 was used instead of $-\infty$ for practical purpose

Table 4: Various Parameters

Parameter	Value	Parameter	Value
Circuitry		**Chemical Energy**	
R_L	3.1 kΩ	σ	0.01 J/m^3
$V_{\text{amp(+ve)}}$, $V_{\text{amp(-ve)}}$	1.25 V, -1.75 V	$\overline{\delta\mu_1}$	10 GJ/m^3
		$\overline{\delta\mu_2}$	6.5 GJ/m^3
λ	100 V/s, 10 kV/s, 1 MV/s	β_1	0.35 GJ/m^3
		β_2	0.5 GJ/m^3
		ΔW_{Buc}	1.0 eV
Filament Nucleation		ΔW_{Bi}	ΔW_{Bi}
h	5 nm	ΔW_{Bmc}	0.01 J/m^3
W_0	2.5 eV	**Static Disorder**	
Λ	6.6	σ_{0f}	rand(2, 8) kS/m[g]
r_c	2.9 nm	σ_{0g}	rand(1, 5) kS/m[g]
r_{min}	0.5nm	α_f	rand(-0.07, -0.03)[g]
α	$r_{\text{min}}/r_{\text{c}}$	α_g	rand(0.03, 0.07)[g]
Electric Conductivity		$\overline{\delta\mu_1}$	rand(8.5, 11.5) GJ/m^3[g]
σ_{0f}	5 kS/m	$\overline{\delta\mu_2}$	rand(5.5, 7.5) GJ/m^3[g]
σ_{0g}	3 kS/m	W_0	rand(2.4, 2.6) eV[g]
α_f	-0.05	**Thermal Conductivity**	
α_g	0.05	κ_{eff}	10
τ	V_{amp}/λ	[g] function rand(x, y) produces uniformly distributed random number between x and y	
$\tau_0(\tau_{\text{min}})$	0.1 ps		